

Elucidating the mechanism of step-emulsification

Andrea Montessori ^{*1}, Marco Lauricella¹, Sauro Succi^{2,1,3}, Elad Stolovicki⁴, and David Weitz^{4,5}

¹Istituto per le Applicazioni del Calcolo CNR, via dei Taurini 19, Rome, Italy

²Center for Life Nano Science@La Sapienza, Istituto Italiano di Tecnologia, 00161 Roma, Italy

³Institute for Applied Computational Science, Harvard John A. Paulson School of Engineering And Applied Sciences, Cambridge, MA 02138, United States

⁴School of Engineering and Applied Sciences, Harvard University, McKay 517 Cambridge, MA 02138, USA

⁵Department of Physics, and School of Engineering and Applied Sciences, Harvard University, Pierce 231, 29 Oxford St. Cambridge, MA 02138, USA

June 22, 2020

Abstract

Three-dimensional, time-dependent direct simulations of step emulsification micro-devices highlight two essential mechanisms for droplet formation: first, the onset of an adverse pressure gradient driving a back-flow of the continuous phase from the external reservoir to the micro-channel. Second, the striction of the flowing jet which leads to its subsequent rupture. It is also shown that such a rupture is delayed and eventually suppressed by increasing the flow speed of the dispersed phase within the channel, due to the stabilising effect of dynamic pressure. This suggests a new criterion for dripping-jetting transition, based on local values of the Capillary and Weber numbers.

Step emulsification (SE) has captured significant interest in the recent years as a viable microfluidic technique for the controlled production of liquid droplets [1, 2]. Among others, one of the main appeals of the SE technique is the prospect of producing large volume rates of the dispersed phase, which are out of reach for previous techniques, such as flow-focusers [3, 4, 5, 6].

The basic idea behind SE is to exploit the pressure drop due to a sudden channel expansion (step) to induce the pinch-off of the dispersed phase, leading to droplet formation [7]. Albeit conceptually straightforward, the details of the process depend on a number of physical and geometrical parameters, primary the capillary number Ca and the aspect ratio h/w of the height versus width of the micro channel cross-section (see Figure 1). Such parameters dictate the shape of the droplet and the transition between the dripping and the jetting regimes [7, 8, 9]. Although of primary importance, the Capillary number (viscous dissipation/surface tension) does not capture the full picture and needs to be complemented by other dimensionless groups, namely the Weber number (inertia/surface tension) and/or Reynolds numbers (inertia/viscous dissipation).

Despite major technological advances, the theoretical description and the numerical simulation of micro-channel emulsification is still under development.

In this Letter, we present direct numerical simulations of the fully three-dimensional, time-dependent Navier-Stokes equations for a specific step-emulsification micro-device, in order to elucidate the basic fluid phenomena underpinning the step-emulsification process. The simulations highlight two essential mechanisms: i) the back-flow of the continuous phase from the external reservoir to the confined micro channel, driven by an adverse pressure gradient, ii) the resulting striction of the flowing jet within the channel and its subsequent rupture. It is also shown that such a rupture is delayed or even suppressed upon increasing the flow speed of the dispersed phase within the channel, due to the stabilising effect of dynamic pressure.

In order to simulate the droplet breakup in a recently proposed class of step emulsification devices [10, 2, 8] we solve the multi-component Navier-Stokes equations, using an extensions of the Lattice Boltzmann method [11, 12, 13, 14, 15, 16, 17]. See Supplemental Material at 2 for a detailed description of the numerical model employed [18, 19, 20]. The device, made of polydimethylsiloxane (PDMS), is used for producing water in oil emulsions and a sketch is reported in figure 1. The water flows through the device inlet, and splits into hundreds of step-emulsifier nozzles with rectangular cross sections. The PDMS device is submerged in quiescent oil, the continuous phase, with the nozzles pointing upwards. The dispersed phase (water), is then pumped through

*Electronic address: and.montessori@gmail.com; Corresponding author

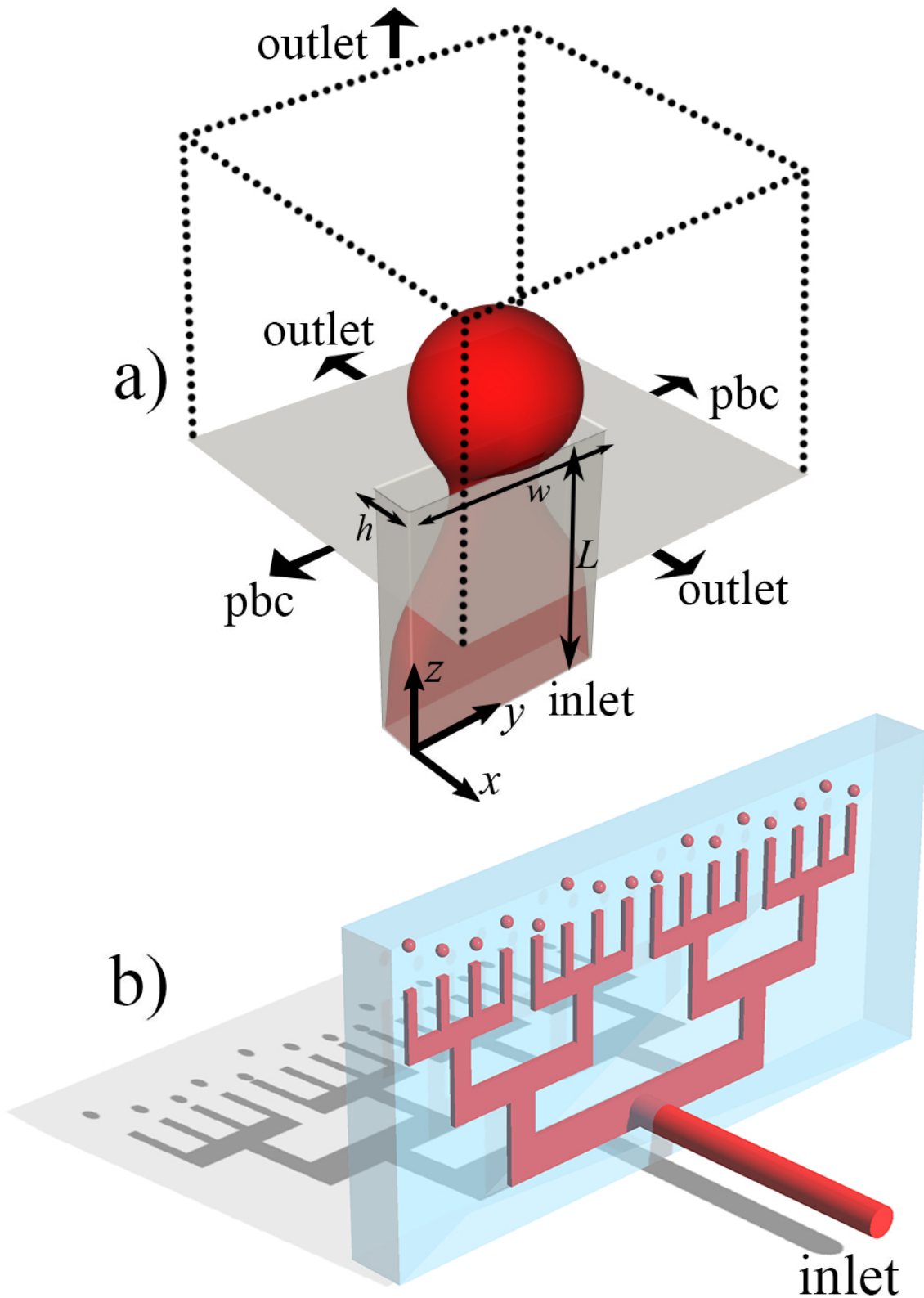


Figure 1: Sketch of the nozzle geometry in the simulation box, along with the imposed boundary conditions (top panel a). The adopted conditions reproduce a periodic array of independent nozzles, which is consistent with the geometry of the volcano device (bottom panel b). Here, the dispersed phase (red) is pumped through the device, forming mono-disperse drops in a reservoir containing a continuous immiscible phase (cyan).

the device and forms monodisperse drops, whose sizes are proportional to the nozzle height (h). We wish to point out that, being the device submerged in quiescent oil, there is no net flow of the continuous phase, this in contrast with the emulsification system employed in [21]. In this work, we simulate a single nozzle out of

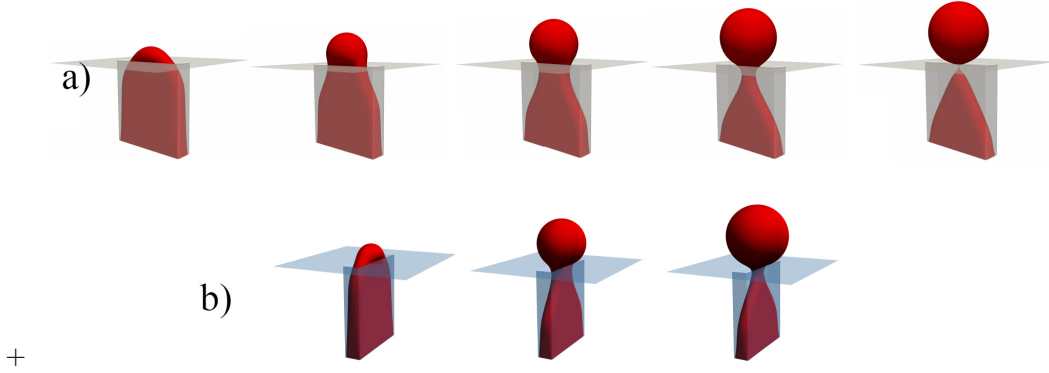


Figure 2: a) sequence of the break process in the dripping regime in a step emulsification nozzle. The dispersed phase (water), is pumped through the device and forms monodisperse drops whose sizes are proportional to the nozzle height. b) Sequence of the step emulsifier in the jetting regime

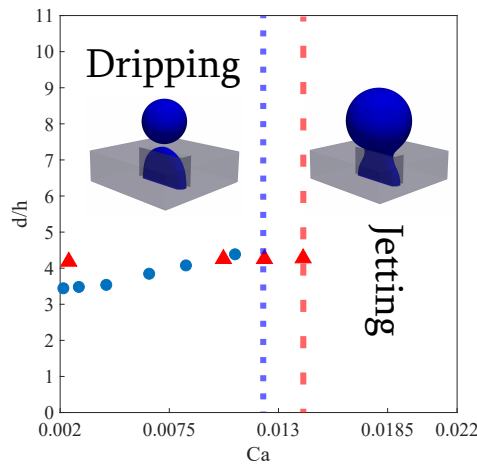


Figure 3: Dimensionless droplet diameter (d/h) versus the Capillary number for a nozzle aspect ratio $h/w = 1/5$. The dots are the normalized droplet diameters predicted by the numerical simulations, while the triangles stand for the experimental values of the normalized diameters. In the dripping region, for Ca between 0.002 and $\mathcal{O}(10^{-2})$ the average value of the droplet diameter is $\sim 540\mu\text{m}$ ($d/h \sim 4$). The vertical dashed (experimental) and dotted (numerical) lines denote the critical Capillary numbers which mark the dripping to jetting transition.

the full device, using periodic boundary conditions along crossflow directions, in order to mimic the effect of neighbouring nozzles. At the inlet, we impose uniform velocity profiles, while a zero gradient approximation is applied at the outlet. The ratio between the kinematic viscosities of the dispersed and the continuous phase is fixed to ~ 1.2 , as in [8],¹ [22, 23, 24, 25].

First, we perform a comparison with the experiments reported in [8], by investigating the effect of the main non-dimensional parameters i.e., the capillary number ($Ca = \rho U \nu / \sigma$) and the Weber number ($We = \rho U^2 L / \sigma$), where U is the velocity of the dispersed phase at the inlet, ρ is the density of the dispersed phase, L is a characteristic length defined as \sqrt{wh} (see fig. 1), σ is the oil-water surface tension and ν is the kinematic viscosity of the dispersed phase.

In our simulations the dispersed phase flows through nozzles with a rectangular cross section of $135 \times 700\mu\text{m}^2$ and length $L = 810\mu\text{m}$, with a characteristic nozzle aspect ratio $h/w = 1/5$, being h and w the height and the width of the microchannel, respectively. Experiments show that the droplet sizes are nearly independent of the flow rate over an extended range (between 12 and 70 mL/min , $0.002 < Ca < 0.014$) with an average drop diameter of $d = 567 \pm 6\mu\text{m}$. In this range of flow rates, thus for Capillary numbers in the range $\mathcal{O}(10^{-3}) \div \mathcal{O}(10^{-2})$, the step emulsifier has been shown to operate in the dripping regime, while for larger flow rates, i.e. for Capillary numbers larger than a critical value, a transition from dripping to jetting regime occurs, which is characterized by the production of much larger and polydisperse droplets [2, 10]. The dripping-jetting transition occurs whenever the droplet does not break up anymore and starts 'ballooning' (i.e., above a critical

¹We performed additional simulations in which the same range of capillary numbers was spanned by changing the viscosity ν and or the surface tension σ . The simulation results show that the transition from dripping to jetting occurs almost at the same critical Capillary number, corresponding to lower flow rates as the viscosity of the inner phase is increased.

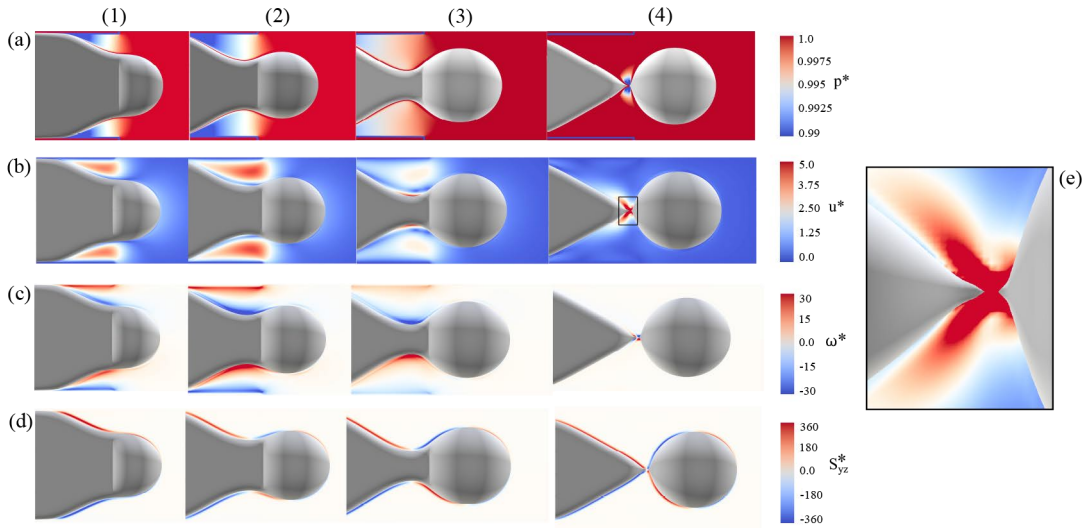


Figure 4: (a) Pressure (p^*), (b) velocity (u^*), (c) vorticity (ω^*) and (d) stress fields (S_{yz}^*), in a y - z midplane taken between the two walls separated by h , from the focusing stage (1,2) to the pinching (3) and finally breakup (4). (e) Zoom of the droplet structure and associated flow field at breakup time. In this simulation $Ca = 0.003$ and $h/w = 1/5$.

Capillary number the newborn droplet grows larger and larger, see fig. 2. The simulations exhibit a satisfactory agreement with the experimental results, as shown in fig 3. First, in the dripping region ($0.002 < Ca < 0.0125$) the average droplet diameter is $d \sim 540\mu m$ ($d/h \sim 4$), in satisfactory agreement with the experimental data [8], see fig. 3.

The numerical simulations also predict a critical Capillary number $Ca \sim 0.0125$, which is in good agreement with experimental observations [8, 10] (see fig. 3). It is worth noting that, by scanning the capillary number, we encompass a broad range of conditions associated with different values of the physical properties, such as dynamic viscosity, surface tension, as well as operational parameters, such as the flow rate.

Figure 4 collects the main results of the present analysis. In the top panel (a) we show a time-sequence of the pressure field from the focusing stage (1,2) to the pinching (3) and finally breakup (4). This sequence unveils the following picture: the continuous phase flows back from the external reservoir to the confined micro channel (focusing stage) and the flowing jet ruptures as a consequence of the striction induced by such backflow. Note that the rupture is driven by the negative curvature which develops in the striction region (pinching stage).

In panel (b), we show the magnitude of the flow field, scaled with the inlet velocity. In figures b1 and b2, the build-up of a significant back flow is apparent, amounting to about three times the inlet velocity. As the pinching progresses, the backflow speed decreases, due to the enlarged section available to the continuum phase. At breakup time, a very localised burst is observed, signalling the rupture of the jet. In panel e) we zoom into the structure of the droplet and associated flow field at breakup time. Such figure clearly shows the re-entrant motion of the jet, accompanied by the rapid acceleration of the newborn droplet.

In panel (c) we show the time-sequence of the vorticity field, in units of U/h . This sequence displays a typical elongational flow structure, especially in figure 4, panel c3, which stretches the jet until rupture.

Finally, in panel (d) we show the component of the stress field in the yz mid-plane, in units of U/h . The sequence shows that the stress field is highly localised around the oil-water interface, with a null-point right at the pinch position [26]. The present analysis is in line with previous studies [27], in which the breakup is not interpreted as due to a Plateau-Rayleigh instability [28], but rather to the back flow of the continuum phase, triggered by the adverse pressure gradient which arises in correspondence with the focusing of the water jet. We wish to emphasize that our analysis is fully dynamic and three-dimensional, i.e it does not rely on any quasi-static assumption [7], nor on any axial-symmetry of the flow [29].

Dripping to jetting transition.

Most experimental studies of step-emulsification report a dripping to jetting transition above a critical capillary number $Ca_{crit} \sim \mathcal{O}(10^{-2})$ [1, 8, 10]. However, the underlying mechanisms behind such transition are still under investigation. Here, we wish to point out that the transition to the jetting regime is facilitated by the contribution of the dynamic pressure $\rho_{in}u_{in}^2/2$, being ρ_{in} and u_{in} the local density and velocity of the dispersed phase in the pinching region. Such dynamic pressure withstands the effects of the negative-curvature in the pinch region. Due to the pinching effect, the local flow speed within the dispersed phase significantly exceeds the inlet velocity. Hence, the local capillary number attains larger values, of the order of $0.1 - 1$, whenever the nominal capillary number of the dispersed phase reaches its critical value around 0.01. Note that the nominal

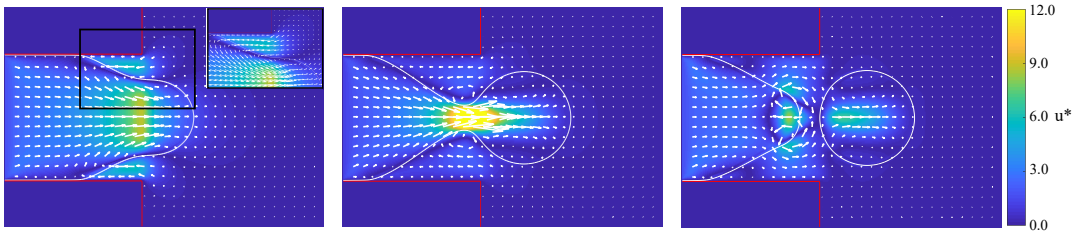


Figure 5: Normalized velocity magnitude and vector field in the dripping nozzle. The counterflow in the continuous phase within the nozzle, is clearly evidenced by the quiver plot. The solid white line identifies the interface between the continuous and the dispersed phase while the red line denotes the walls of the nozzle. The inset in the leftmost panel, highlights the backflow occurring inside the nozzle.

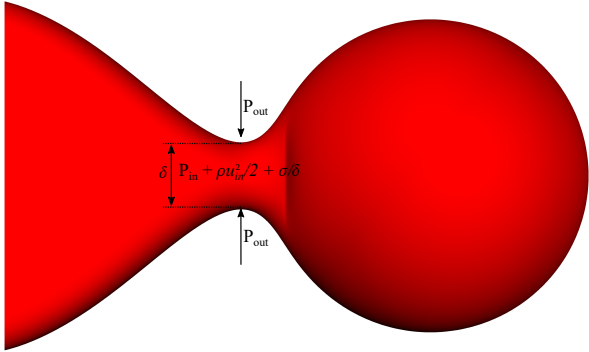


Figure 6: Sketch of the static and dynamic pressure components in and out of the neck region.

capillary number is computed with the imposed velocity at the inlet.

The local acceleration of the flow field inside the pinch region is clearly visible in Figure 5, which reports the flow field inside the neck region of the dispersed phase.

As pinching progresses in time, the flow speed inside the pinching region grows accordingly, so that, at some point, inertial effects can no longer be neglected.

To clarify the point, let us write the dynamic force balance under flow conditions, namely:

$$P_{in} + \rho_{in}u_{in}^2/2 = P_{out} + \rho_{out}u_{out}^2/2 - \frac{\sigma}{\delta} \quad (1)$$

where subscripts "in" and "out" refer to the neck region (see fig.6), inside and outside the water jet, respectively. Note that the minus sign in front of the surface tension reflects the negative curvature (see fig. 6).

In equation 1, δ is the characteristic length scale of the neck region, which is found to be smaller but comparable with the channel height h . This is plausible, because $\delta > h$ is not feasible since the neck diameter cannot be larger than the height of the nozzle, while $\delta \ll h$ signals the imminent breakup.

This expression shows that the inner dynamic pressure adds to the surface tension in withstanding the outer pressure. As a result, it is natural to extend the definition of Capillary number so as to include the contribution of the dynamic pressure, namely:

$$K = \frac{\mu u_{in}}{\sigma + \rho u_{in}^2 \delta / 2} \equiv \frac{Ca_{in}}{1 + We_{in}} \quad (2)$$

where we have neglected the outer velocity since $u_{out}/u_{in} \sim \delta/w < 1$.

For the case of figure 4, we have $Ca_{in} = 0.015$ and $We_{in} \sim 0.22$, showing that the dynamic pressure is still sub-dominant with respect to the capillary pressure σ/δ . On the other hand, in the case of jetting, (see panel (c) in Fig. 2) $We_{in} \sim 1$, indicating that the jetting regime is entered whenever the dynamic pressure becomes comparable or higher than the capillary pressure.

We wish to point out that since $\delta \sim h$, $Ca_{in} \sim \frac{w}{h} Ca$, which is precisely the quantity controlling the dripping-jetting criterion discussed in [21]. In this Letter, we noted that such criterion should also take into account the contribution of dynamic pressure, which becomes dominant in the pinch region.

1 Acknowledgments

The research leading to these results has received funding from the European Research Council under the European Union's Horizon 2020 Framework Programme (No. FP/2014- 2020)/ERC Grant Agreement No. 739964 ("COPMAT").

2 Supplementary information

The LB immiscible multicomponent model is based on the following lattice Bhatnagar-Gross-Krook (BGK) equation:

$$f_i^k(\vec{x} + \vec{c}_i \Delta t, t + \Delta t) = f_i^k(\vec{x}, t) + \Omega_i^k(f_i^k(\vec{x}, t)), \quad (3)$$

where f_i^k is the discrete distribution function, representing the probability of finding a particle of the k -th component at position \vec{x} and time t with discrete velocity \vec{c}_i . The lattice time step is taken equal to 1, and i the index spans the lattice discrete directions $i = 0, \dots, b$, where $b = 26$ for a two dimensional nine speed lattice (D3Q27). The density ρ^k of the k -th fluid component is given by the zeroth order moment of the distribution functions

$$\rho^k(\vec{x}, t) = \sum_i f_i^k(\vec{x}, t), \quad (4)$$

while the total momentum $\rho \vec{u}$ is defined by the first order moment:

$$\rho \vec{u} = \sum_i \sum_k f_i^k(\vec{x}, t) \vec{c}_i. \quad (5)$$

The collision operator Ω_i^k results from the combination of three sub-operators, namely [16]

$$\Omega_i^k = (\Omega_i^k)^{(3)} \left[(\Omega_i^k)^{(1)} + (\Omega_i^k)^{(2)} \right]. \quad (6)$$

Here, $(\Omega_i^k)^{(1)}$ is the standard BGK operator for the k -th component, accounting for relaxation towards a local equilibrium

$$(\Omega_i^k)^{(1)} f_i^k(\vec{x}, t) = f_i^k(\vec{x}, t) - \omega_k \left(f_i^k(\vec{x}, t) - f_i^{k,eq}(\vec{x}, t) \right), \quad (7)$$

where ω_k is the relaxation rate, and $f_i^{k,eq}(\vec{x}, t)$ denotes local equilibria, defined by

$$f_i^{k,eq}(\vec{x}, t) = \rho^k w_i \left(1 + \frac{\vec{c}_i \cdot \vec{u}}{c_s^2} + \frac{(\vec{c}_i \cdot \vec{u})^2}{2c_s^4} - \frac{(\vec{u})^2}{2c_s^2} \right) \quad (8)$$

Here, w_i are weights of the discrete equilibrium distribution functions, $c_s = 1/\sqrt{3}$ is the lattice sound speed [?]. In this model, $(\Omega_i^k)^{(2)}$ is a perturbation operator, modeling the surface tension of the k -th component. Denoting by \vec{F} the color gradient in terms of the color difference (see below), this term reads

$$(\Omega_i^k)^{(2)} f_i^k(\vec{x}, t) = f_i^k(\vec{x}, t) + A_k |\vec{F}| \left[w_i \frac{(\vec{F} \cdot \vec{c}_i)^2}{|\vec{F}|^2} - B_i \right], \quad (9)$$

with the free parameters A_k modeling the surface tension, and B_k a parameter depending on the chosen lattice [17, 18]. The above operator models the surface tension, but it does not guarantee the immiscibility between different components. In order to minimize the mixing of the fluids, a recoloring operator $(\Omega_i^k)^{(3)}$ is introduced. Following the approach in Ref. [18], being ζ and ξ two immiscible fluids, the recoloring operators for the two fluids read as follows

$$\begin{aligned} (\Omega_i^\zeta)^{(3)} &= \frac{\rho^\zeta}{\rho} f_i + \beta \frac{\rho^\zeta \rho^\xi}{\rho^2} \cos(\phi_i) \sum_{k=\zeta, \xi} f_i^{k,eq}(\rho^k, 0) \\ (\Omega_i^\xi)^{(3)} &= \frac{\rho^\xi}{\rho} f_i - \beta \frac{\rho^\zeta \rho^\xi}{\rho^2} \cos(\phi_i) \sum_{k=\zeta, \xi} f_i^{k,eq}(\rho^k, 0) \end{aligned} \quad (10)$$

where β is a free parameter and $\cos(\phi_i)$ is the cosine of the angle between the color gradient \vec{F} and the lattice direction \vec{c}_i . Note that $f_i^{k,eq}(\rho^k, 0)$ stands for the set of equilibrium distributions of k -th fluid evaluated setting the macroscopic velocity to zero. In the above equation, $f_i = \sum_k f_i^k$. The LB color gradient model has been enriched with the so called regularization procedure [19, 20, ?], namely a discrete Hermite projection of the post-collisional set of distribution functions onto a proper set of Hermite basis. The main idea is to introduce

a set of pre-collision distribution functions which are defined only in terms of the macroscopic hydrodynamic moments. All the higher-order non-equilibrium information, often referred to as *ghosts* [12], is discarded. In equations, the regularized LB reads as follows:

$$f_i^k(x_i + c_i \Delta t, t + \Delta t) = \mathcal{R} f_i^{k, neq}(x, t) \equiv f_i^{k, eq} - \Delta t \omega_k (f_i^{k, reg} - f_i^{k, eq}) \quad (11)$$

where $f_i^{k, reg}$ is the hydrodynamic component of the full distribution f_i^k (see [20]) for the k -th color, and \mathcal{R} is the regularization operator. The above equation shows that the post-collision distribution, of a 4th-order isotropic lattice, is defined only in terms of the conserved and the transport hydrodynamic modes, namely density ρ , current $\rho \vec{u}$ and momentum-flux tensor $\mathbf{\Pi} = \sum_i f_i \vec{c}_i \vec{c}_i$.

References

- [1] S. Sugiura, M. Nakajima, N. Kumazawa, S. Iwamoto, M. Seki, Characterization of spontaneous transformation-based droplet formation during microchannel emulsification, *The Journal of Physical Chemistry B* 106 (36) (2002) 9405–9409. doi:10.1021/jp0259871.
URL <https://doi.org/10.1021/jp0259871>
- [2] C. Priest, S. Herminghaus, R. Seemann, Generation of monodisperse gel emulsions in a microfluidic device, *Applied Physics Letters* 88 (2) (2006) 024106. doi:10.1063/1.2164393.
URL <https://doi.org/10.1063/1.2164393>
- [3] P. Garstecki, H. A. Stone, G. M. Whitesides, Mechanism for flow-rate controlled breakup in confined geometries: A route to monodisperse emulsions, *Physical review letters* 94 (16) (2005) 164501.
- [4] P. Garstecki, M. J. Fuerstman, H. A. Stone, G. M. Whitesides, Formation of droplets and bubbles in a microfluidic t-junction-scaling and mechanism of break-up, *Lab on a Chip* 6 (3) (2006) 437–446.
- [5] M. Costantini, C. Colosi, P. Mozetic, J. Jaroszewicz, A. Tosato, A. Rainer, M. Trombetta, W. Świąszkowski, M. Dentini, A. Barbetta, Correlation between porous texture and cell seeding efficiency of gas foaming and microfluidic foaming scaffolds, *Materials Science and Engineering: C* 62 (2016) 668–677.
- [6] S. L. Anna, N. Bontoux, H. A. Stone, Formation of dispersions using "flow focusing" in microchannels, *Applied physics letters* 82 (3) (2003) 364–366.
- [7] R. Dangla, E. Fradet, Y. Lopez, C. N. Baroud, The physical mechanisms of step emulsification, *Journal of Physics D: Applied Physics* 46 (11) (2013) 114003.
- [8] E. Stolovicki, R. Ziblat, D. A. Weitz, Throughput enhancement of parallel step emulsifier devices by shear-free and efficient nozzle clearance, *Lab on a Chip* (2018). doi:10.1039/c7lc01037k.
URL <http://dx.doi.org/10.1039/c7lc01037k>
- [9] A. Ofner, D. G. Moore, P. A. RÅEhs, P. Schwendimann, M. Eggersdorfer, E. Amstad, D. A. Weitz, A. R. Studart, High-throughput step emulsification for the production of functional materials using a glass microfluidic device, *Macromolecular Chemistry and Physics* 218 (2) (2017) 1600472–n/a, 1600472. doi:10.1002/macp.201600472.
URL <http://dx.doi.org/10.1002/macp.201600472>
- [10] N. Mittal, C. Cohen, J. Bibette, N. Bremond, Dynamics of step-emulsification: From a single to a collection of emulsion droplet generators, *Physics of Fluids* 26 (8) (2014) 082109. doi:10.1063/1.4892949.
URL <https://doi.org/10.1063/1.4892949>
- [11] A. Montessori, M. Lauricella, M. La Rocca, S. Succi, E. Stolovicki, R. Ziblat, D. Weitz, Regularized lattice boltzmann multicomponent models for low capillary and reynolds microfluidics flows, *Computers & Fluids* 167 (2018) 33 – 39. doi:<https://doi.org/10.1016/j.compfluid.2018.02.029>.
URL <http://www.sciencedirect.com/science/article/pii/S0045793018300926>
- [12] F. Higuera, S. Succi, R. Benzi, Lattice gas dynamics with enhanced collisions, *EPL (Europhysics Letters)* 9 (4) (1989) 345.
- [13] A. Montessori, P. Prestininzi, M. La Rocca, S. Succi, Lattice boltzmann approach for complex nonequilibrium flows, *Physical Review E* 92 (4) (2015) 043308.
- [14] R. Benzi, M. Sbragaglia, S. Succi, M. Bernaschi, S. Chibbaro, Mesoscopic lattice boltzmann modeling of soft-glassy systems: theory and simulations, *The Journal of Chemical Physics* 131 (10) (2009) 104903.

- [15] S. Succi, *The Lattice Boltzmann Equation: For Complex States of Flowing Matter*, Oxford University Press, 2018.
- [16] S. Leclaire, M. Reggio, J.-Y. Trépanier, Numerical evaluation of two recoloring operators for an immiscible two-phase flow lattice boltzmann model, *Applied Mathematical Modelling* 36 (5) (2012) 2237–2252.
- [17] T. Reis, T. Phillips, Lattice boltzmann model for simulating immiscible two-phase flows, *Journal of Physics A: Mathematical and Theoretical* 40 (14) (2007) 4033.
- [18] S. Leclaire, M. Reggio, J.-Y. Trépanier, Isotropic color gradient for simulating very high-density ratios with a two-phase flow lattice boltzmann model, *Computers & Fluids* 48 (1) (2011) 98–112.
- [19] A. Montessori, G. Falcucci, P. Prestininzi, M. La Rocca, S. Succi, Regularized lattice bhatnagar-gross-krook model for two-and three-dimensional cavity flow simulations, *Physical Review E* 89 (5) (2014) 053317.
- [20] R. Zhang, X. Shan, H. Chen, Efficient kinetic method for fluid simulation beyond the navier-stokes equation, *Physical Review E* 74 (4) (2006) 046703.
- [21] Z. Li, A. Leshansky, L. Pismen, P. Tabeling, Step-emulsification in a microfluidic device, *Lab on a Chip* 15 (4) (2015) 1023–1031.
- [22] I. Kobayashi, S. Mukataka, M. Nakajima, Effects of type and physical properties of oil phase on oil-in-water emulsion droplet formation in straight-through microchannel emulsification, experimental and cfd studies, *Langmuir* 21 (13) (2005) 5722–5730.
- [23] M. Stoffel, S. Wahl, E. Lorenceau, R. Höhler, B. Mercier, D. E. Angelescu, Bubble production mechanism in a microfluidic foam generator, *Physical review letters* 108 (19) (2012) 198302.
- [24] K. van Dijke, I. Kobayashi, K. Schroën, K. Uemura, M. Nakajima, R. Boom, Effect of viscosities of dispersed and continuous phases in microchannel oil-in-water emulsification, *Microfluidics and nanofluidics* 9 (1) (2010) 77–85.
- [25] G. T. Vladislavljević, I. Kobayashi, M. Nakajima, Effect of dispersed phase viscosity on maximum droplet generation frequency in microchannel emulsification using asymmetric straight-through channels, *Microfluidics and Nanofluidics* 10 (6) (2011) 1199–1209.
- [26] J. Eggers, Universal pinching of 3d axisymmetric free-surface flow, *Phys. Rev. Lett.* 71 (1993) 3458–3460.
doi:10.1103/PhysRevLett.71.3458.
URL <https://link.aps.org/doi/10.1103/PhysRevLett.71.3458>
- [27] V. van Steijn, C. R. Kleijn, M. T. Kreutzer, Flows around confined bubbles and their importance in triggering pinch-off, *Physical review letters* 103 (21) (2009) 214501.
- [28] J. Eggers, E. Villermaux, Physics of liquid jets, *Reports on Progress in Physics* 71 (3) (2008) 036601.
URL <http://stacks.iop.org/0034-4885/71/i=3/a=036601>
- [29] I. Chakraborty, J. Ricouvier, P. Yazhgur, P. Tabeling, A. Leshansky, Microfluidic step-emulsification in axisymmetric geometry, *Lab on a Chip* 17 (21) (2017) 3609–3620.